Advances in Engineering Software 173 (2022) 103198

Contents lists available at ScienceDirect

Advances in Engineering Software

journal homepage: www.elsevier.com/locate/advengsoft

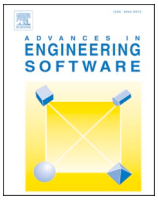

Intelligent decision support system for cardiovascular risk prediction using hybrid loss deep joint segmentation and optimized deep learning

V. Srilakshmi [a,*], K. Anuradha [a], C. Shoba Bindu [b]

[a] Department of CSE, GRIET, Hyderabad, Telangana 500090, India
[b] Department of CSE, JNTU, Anantapur, Andhra Pradesh 515002, India

ARTICLE INFO

Keywords:
Deep joint segmentation
Cardiovascular risk prediction
Deep neuro-fuzzy network
Grayscale conversion
Binarization and circle fixing

ABSTRACT

Cardiovascular disease (CVD) represents an emerging death reason worldwide. CVD is based on the capability to discover the high-risk individuals before designing overt events. An effective technique for CVD risk prediction is developed using retinal fundus images. Initially, the retinal fundus images are subjected to pre-processing using grayscale conversion. The optic disc is detected with binarization and circle fixing. Then, the blood vessel segmentation uses deep joint segmentation, wherein dice coefficient and binary cross-entropy are integrated. After that, the feature extraction is done for mining convenient features that include several statistical features. Meanwhile, features like Local Directional Texture Pattern (LDTP) and Local Gabor Binary Pattern (LGBP) are mined from the inputted image. Then, the cardiovascular risk prediction is made by a Deep neuro-fuzzy network (DNFN), such that the risks are classified into normal and hypertensive. Finally, the DNFN is trained using the developed Fractional Calculus-Horse Herd Optimization Algorithm (FC—HOA), which is devised by combining Fractional Calculus (FC) and the Horse Herd Optimization algorithm (HOA). The proposed FC—HOA-based DNFN offered enhanced efficiency with the highest accuracy, sensitivity and specificity of 91.6, 92.3 and 91.9%.

1. Introduction

CVD is an emerging reason of death all over the world. To stop heart attacks or undesirable cardiovascular events, it becomes essential to determine complete hazards splitted into modifiable and non-modifiable aspects. In the regular clinical setting, several clinicians used risk calculators, like Framingham [1,2], Pooled Cohort equations [3], and SCORE [4,5] to forecast the future risks of cardiovascular diseases. The major risk aspects involve diabetes mellitus, cigarette smoking, Hypertension, and cigarette smoking, leading to huge alterations in several organs and body tissue, like blood vessels, eyes, and kidneys [6]. The current standard of care to screen for CVD risks [7] needs a huge class of variables acquired from the history of patient and blood samples, like blood pressure, age, smoking, and gender. Most cardiovascular risk computations utilize the integration of these attributes to discover the risk of patients who experience whichever cardiovascular [8] occurrence and cardiac based mortality over a specific period. Still, some of these attributes can be unavailable [9]. In addition, the eye is an organ that permits straight visualization of specific non-invasive imaging modalities with neuro-vasculature that offers precious micro-structural changes, which lead to macro-vascular diseases, like stroke and heart diseases. It is observed that the criterions linked with CVD are cholesterol emboli and hypertensive retinopathy, which can be evident in the eye [10].

The retina is generally inspected to screen complexities of particular CVD owing to its individuality in which blood vessels such as they are visible directly without invasive interventions or radiation. Using images, the arithmetical factor of retinal vasculature, like curvature tortuosity, diameter and angles of branching, are evaluated to evaluate CVD, and diabetes. The retinal vessel diameters are observed to be linked with cognitive ability in the older population [11–13]. Retinal photographs offer data regarding human vasculature and provide illustrations of cardiovascular health. Huge population studies have observed that retinal vascular damage and subtle alterations can predict CVD disease and death rates [14]. Automatic segmentation techniques for the retinal vessel segmentation process based on convolution neural networks can be kept with vessel morphological data. By executing the technique, a technique can understand features from the database, which helps to prevent over fitting. CVD prevention is based on the capability to discover individuals with elevated risk before designing explicit events. This focuses on the requirement for precise stratification of risks. An emerging count of new biomarkers is determined to predict

* Corresponding author.
E-mail address: potlurisrilakshmi@gmail.com (V. Srilakshmi).

https://doi.org/10.1016/j.advengsoft.2022.103198
Received 21 March 2022; Received in revised form 16 June 2022; Accepted 23 July 2022
Available online 26 August 2022

CVD events. Here, the biomarkers play an imperative role in defining, prognostication and making a decision concerning the administration of cardiovascular events [15].

Deep learning (DL) represents an ancestor of machine-learning models featured by several evaluation layers that permit a technique for learning the suitable predictive features based on samples despite features hand-engineered. In recent days, the deep convolution neural networks are termed as an imperative kind of deep learning model, which are optimized for images and are adapted to generate highly precise techniques that treat diseases like diabetic retinopathy and melanoma [16,17] with medical images achieved through expertise [9]. DL models are utilized to predict CVD risk aspects using retinal images [18,10]. DL has observed its feasibility in various medical tools, like imaging and diagnostics. Particularly, in medical images, deep learning is a tremendous ability which can be utilized to discover and segment objects in 3-dimensional (3D) images. The major benefit is that DL can mechanize complex analysis that radiologists could perform priory and is reliable at scale with high speed and less cost. It made DL an emerging model to automate the prediction of cardiovascular occurrence from the images. The commonality of the systems should be revealed as they require forecasting the cardiovascular proceedings of symptomatic and asymptomatic entities amongst several clinical cases and working strongly on data considering various institutions [19].

The main goal is to design a productive model for cardiovascular risk prediction with retinal fundus images using the proposed FC—HOA. First, to eliminate the extra noises present in the image using grayscale conversion the given input image is forwarded to the pre-processing phase. After that, optic disc detection is done with binarization and circle fixing. The next step is to segment the blood vessel from the pre-processed image using deep joint segmentation, wherein dice coefficient and binary cross-entropy are combined for computing distance. Once the segmentation is done, mining features is done to mine appropriate features. After that, cardiovascular risk prediction is effectively made using a DNFN such that the risk is classified into normal and hypertensive types. Finally, the network classifier is trained using the newly projected FC—HOA, devised by an amalgamation of FC into HOA.

The major contributions of the designed model

- *Proposed FC—HOA-based DNFN for cardiovascular risk prediction*: The projected FC—HOA-based DNFN is utilized to predict cardiovascular risk. The output from the proposed FC—HOA-based DNFN is classified as normal and Hypertension.
- *Proposed FC—HOA*: FC—HOA is created by combining FC concept into HOA. It is used to train the DNFN classifier.

The rest of the sections are enlisted below. First, we explain the classical cardiovascular risk prediction methods in Section 2. Then, we have explained the proposed method for predicting the cardiovascular risk in Section 3. Thirdly, we have explained the efficiency of a projected model by comparing it with classical models in Section 4. Finally, discussion about conclusion is given in the Section 5.

2. Motivations

Various methods are used for cardiovascular risk prediction techniques, but observing and analyzing the associations is complex due to many features in real data. Therefore, develop a technique is mainly to overcome the issues and the challenges faced by classical techniques.

2.1. Literature survey

The eight classical cardiovascular risk prediction methods are presented with their pros and cons. Poplin et al. [9] devised a deep model with retinal fundus images for predicting cardiovascular events. Here, cardiovascular risk factors, like gender, smoking status, and systolic blood pressure, were considered for the Evaluation. The method considered limited datasets. To deal with large datasets, Ting et al. [10] developed AI model for predicting cardiovascular risks. The Optical Coherence Tomography (OCT) was considered an effective imaging modality for evaluating CVD. The OCT angiographic alterations serve as a diabetes marker for effective prediction. This technique did not predict long-term cardiovascular risk. To predict long-term cardiovascular risk, Son et al. [13] devised Coronary Artery Calcium score (CACS) for predicting the cardiovascular events using retinal fundus imaging. Here, the efficiency of deep learning model, namely inception-v3 was computed to differentiate the high CACS. This technique was not suitable with heterogeneous databases.To deal with heterogeneous databases, Dai et al. [6] devised deep learning for screening the diabetes and Hypertension using retinal fundus images. The method splitted the image database for improved processing. Fine-tuning of the classifier and last convolution layer of deep residual network was trained by the binary classification model. The method acquired a huge acquisition cost. To minimize acquisition cost, Cheung et al. [20] devised an automated technique for predicting the cardiovascular diseases. The technique performed improved efficiency in predicting the CVD risk factors, including BMI, blood pressure, and hemoglobin levels. The method did not include Inter and Intra-human grader variability. To reduce complexity, Ballinger et al. [21] devised multi-task long short term memory for predicting the cardiovascular disease using fundus images. Here, the two semi-supervised training technique and heuristic pre-training was utilized for processing the tasks. The method suffered from scarcity of labeled data. To minimize data scarcity issue, Zeleznik et al. [19] developed deep learning model for automatically quantifying cardiovascular disease. Here, the automatic score was a strong predictor of cardiovascular events and considered several risk aspects. The method did not discover non-calcified plaque. To discover non-calcified plaque, Rim et al. [14] devised a cardiovascular risk stratification model using DL for predicting the CVD. Here, the DL model was utilized for predicting the probability of existence of CAC. However, the misclassification was a major issue. Mahiddin et al. [7] devised Interrelated Decision-Making Model for an Intelligent Decision Support System (IDM-IDSS-healthcare), which utilized knowledge from previous and ongoing treatment stages. The method is highly efficient. However, the method is very complex. Rahim et al. [8] proposed a Machine Learning based Cardiovascular Disease Diagnosis (MaLCaDD) for the effective prediction of cardiovascular diseases. Here, MaLCaDD method shows high precision and it is highly reliable. However, the method does not share the real time evaluation.

2.2. Major challenges

Problems confronted by existing CVD prediction are enlisted:

- In [9], images with a 45° view were utilized, which is a major issue. In addition, it did not cover extra signals in retinal images, which permits improved CVD risk analysis.
- The DL technique enhances CVD risk analysis [20], which can learn visual structures with images to predict major adverse cardiovascular events (MACE). However, it did not include my effectual features for predicting the risks.
- To effective mine features, deep learning is utilized. However, even though the model attained the highest generalization, such as fine-tuning and data augmentation on test data, it suffered from over-fitting issues and had less training data [6].
- The multi-task LSTM is devised in [21] that automatically predict cardiovascular events with images to deal with over fitting issues. Still, it could not forecast CVD events of symptomatic and asymptomatic individuals in several clinical cases.
- The majority of CVD risk factors utilize an integration of attributes for identifying a patient's risks within a specified time instance. Anyhow, the unavailability of some attributes is considered a major problem.

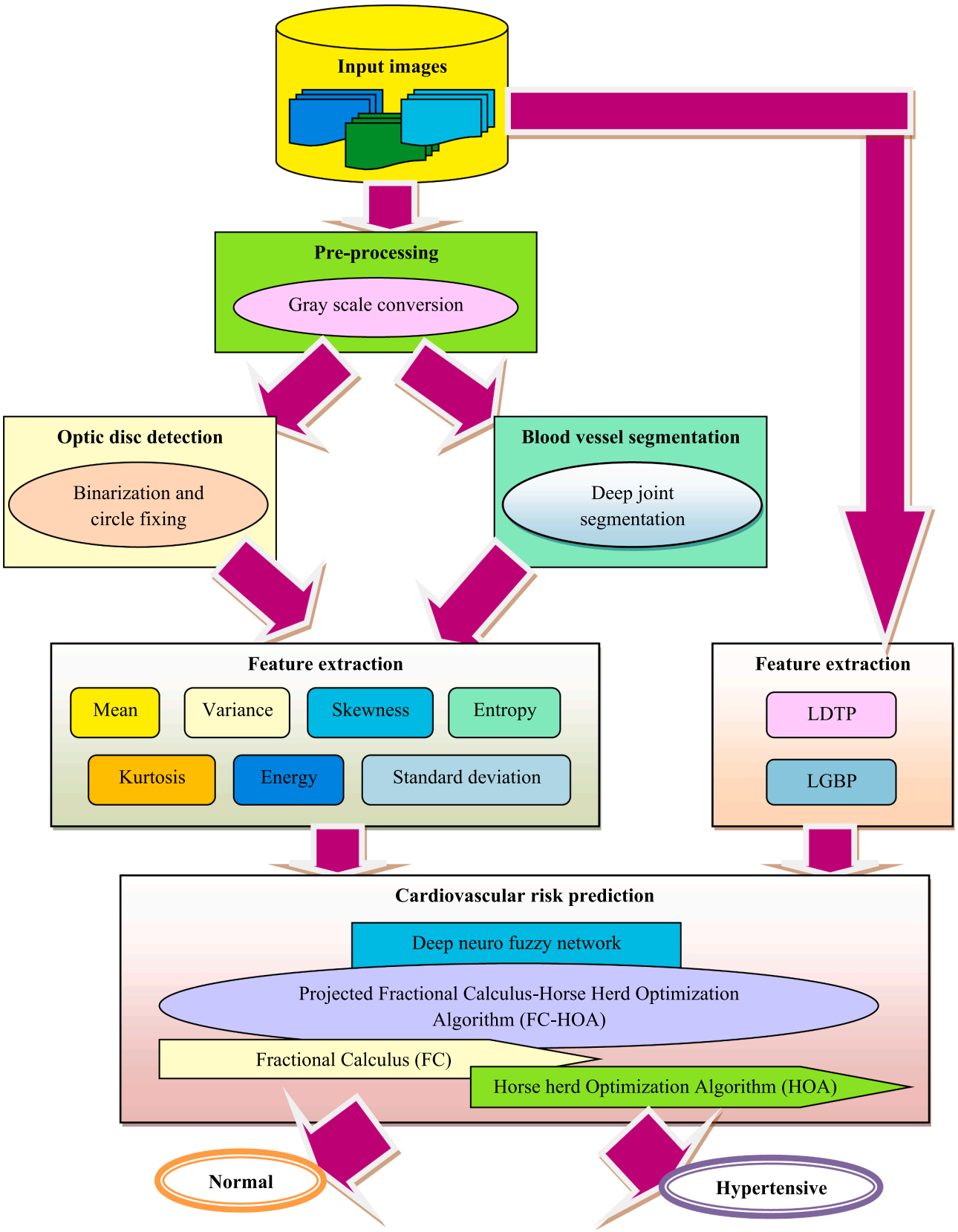

Fig. 1. Structure of cardiovascular disease detection using FC—HOA-based DNFN.

3. Proposed FC—HOA-based DNFN for cardiovascular risk prediction

The clinicians have carried out a fundus inspection amongst patients to discover existence and ruthlessness of retinal damage as way to evaluate cardiovascular disease. The stratification of risk is core part to discover and manage groups at risk for cardiovascular disease that led to huge deaths. The aim is to create a effective technique for predicting cardiovascular risk using retinal fundus images with proposed FC—HOA. The image attained from database indicated in [22] is adapted as an input image for complete processing. The input image is forwarded to pre-processing with grayscale conversion. Then, the optic disc detection is done with binarization and circle fixing [23]. The next step is to segment blood vessel from pre-processed image with deep joint segmentation [24] in which dice coefficient and binary cross-entropy are combined and used instead of MSE. Once the segmentation is done, the feature is mined from pre-processed image, blood vessel segmented image and optic segmented image. Thereafter, cardiovascular risk prediction is effectively done with DNFN [25], such that the risks are classified into normal and hypertensive type. Here, the DNFN is trained with proposed FC—HOA, which is devised by combining FC [26] and HOA [27]. Here, Fig. 1 shows the structure of cardiovascular disease detection using proposed FC—HOA-based DNFN.

3.1. Acquisition of images

Assume a database of the image A with f images and is verbalize as:

$$A = \{J_1, J_2, \ldots, J_r, \ldots, J_f\} \tag{1}$$

where, J_r is r th the input image and f refers to full images.

3.2. Grayscale conversion pre-processing

The input image J_r is adapted to pre-processing in which the conversion of grayscale is performed to maximize the contrast of image. It is essential to pre-process the image, as it helps to increase image clarity. The pre-processing is done with grayscale conversion.

Grayscale conversion: RGB color representation is the additive color model where red, green, and blue lights are utilized in various ways to reproduce huge array of colors. Grayscale conversion is a procedure of evaluating digital image into grayscale values, wherein each pixel represents a single sample. This means that grayscale only comprises intensity data and this type of image is known as black and white, which exclusively composes shades of grey. Here, black indicates weal intensity value in which white indicates strong value of intensity. The grayscale image results in evaluating intensity of light at each pixel in the single band of electromagnetic spectrum. The pre-processed output is given by $J^{'}$.

3.3. Detection of optic disc with circle fixing and binarization

Once the pre-processing is done $J^{'}$, the optic disc detection is done with binarization and circle fitting model. Hence the discovery of optic disc is of huge importance for discovering cardiovascular risks.

(i) Binarization

The optic disc is determined with pre-processed image considering the smooth textures with binarization [23]. Binarization assists in dividing complex regions through the smoother regions by computing pixels values present in the image. The binarization is used to convert greyscale images ranging from 0 to 256 grey levels, which can be 0 or 1. In addition, binarization utilizes thresholding for producing binary images. Here, if pixel's value is higher than the threshold value, it represents an object with one or its background pixel with 0. At last, considering the label, filling pixels built the binary image with black or white color.

(i) Circle fitting

The circle fitting [23] is a provided point group in a plane, considered the main part of image processing. Here, fixing the circle around the optic disc region performed the circle fitting.

Parameters adopted in circle fitting are listed;

(i) R- circle radius.
(ii) Y-Circle's "y"-co-ordinate.
(iii) X- Circle's "x"-co-ordinate.

The optic disc acquired from the binarization and circle fitting is denoted as$K$.

3.4. Blood vessel segmentation using the Deep Joint model

The segmented blood cells are done with the Deep Joint model [24] using the pre-processed output$J^{'}$. It is the process of segmenting the blood cells. The steps of the Deep Joint model are illustrated below.

(a) Illustration of Deep Joint model

The pre-processed output has been fed as an input to lesion segmentation, done with the Deep Joint model [24] to segment blood vessels by computing optimal threshold values. Hence, the pre-processed output is pushed to Deep Joint segmentation model, which discovers the distance is evaluated amongst deep and segmentation points and optimal segments with region similarity. The model provides segments with optimum accuracy and is easy to comprehend. It provides a clear insight into regions to discover the diseased part. The DeepJoint [24] comprises three phases: joining, region fusion, and segmentation point generation. The inputted picture is paired into grids & pixels first, and then attached using the mean and threshold values through the joining phase. After joining, the regions fusion is performed with bi-constraints and region similarities are adapted for determining new means for discovering mapped points. Steps adopted in the Deep Joint model are given below,

***Step 1:* Grids configuration**

Various grids are obtained from the image where each grid has size of 2×2. Collaborating with preprocessing image various grids are produced and are given by:

$$B = \{B_1, B_2, \ldots, B_e, \ldots, B_g\} \tag{2}$$

Where,B_e symbolize$e$th grid image and $g$signifies full grids.

***Step 2:* Joining phase**

After produced grids are obtained, intra grid points are combined with the threshold and values of the mean through the pixels. By taking average values of pixel the mean is evaluated. Hence, particular value of threshold that decides the pixels computes the mean. Thus, 1 is fixed to threshold. The computed average value is,

$$B_j = \frac{\sum_{n=1}^{R} H_n}{R} \tag{3}$$

Where, $H_n$signifies values of a pixel with the grid and the pixel count in the grid B_j. The joining pixels equation is,

$$B_j = \frac{\sum_{n=1}^{R} H_n}{R} \pm \alpha \tag{4}$$

Where α signifies threshold.

***Step 3:* Region fusion phase**

By employing assigned grids, region fusion matrix is produced. For

performing region fusion matrix two conditions need to be satisfied, they are given below

(i) G_g Value of Mean, should be lesser than 3.
(ii) For each gird one grid point is chosen.

From the above conditions the region's similarity determined, which is integrate to determine mapped points. The region similarity is,

$$G_g = \frac{\sum_{w=1}^{I} H_w^X}{H} \tag{5}$$

Where, H_w^X signifies joined pixels and Mexpresses total joined pixels. The grid is combined and makes a pair which is known as mapped points and is expressed by,

$$F = F_1, F_2, \ldots, F_u, \ldots, F_t \tag{6}$$

Where, t signifies the count of mapped points in an image.

***Step 4:* Deep points discovery**

Here, missed pixels determined the deep points. The equation is,

$$E = \{\vartheta_\ell\} \ ; 1 < \ell \leq \kappa \tag{7}$$

Where ϑ_ℓ signifies missed pixels and symbolizes the full count of missed pixels. Thus, by adding missed pixels and mapped pixels we can evaluate the deep points and are given by,

$$\kappa_{points} = E + L_p \tag{8}$$

***Step 5:* Optimal segment detection**

Lastly, providing an iterative method discovered the best segments with deep points. The segmented points given N are chosen arbitrarily. Thus, the lowest distance is,

$$P^{dist} = \sqrt{\sum_{p=1}^{q} \left(N_p - \kappa_{points_p}\right)^2} \tag{9}$$

Continue the process, and points of optimum-segmented are selected with dice coefficient and binary cross-entropy, which is given as,

$$X^{Dis} = \beta * DC + (1-\beta)BC \tag{10}$$

Where, β refers to constant, DCsignifies dice coefficient between N_p and κ_{points}, and BC expresses binary cross-entropy κ_{points}. Lastly, the steps have been continued till a termination criterion is acquired. Assume output generated from the Deep Joint model is the segments expressed as Q.

3.5. Acquisition of features

After obtaining the segments$Q$, each segment is mined the feature. The mining of features guarantees the effectual classification of cardiovascular disease prediction. Here, the features acquired from the input image are LGBP and LDTP, and the features acquired from segments that include statistical features are mined.

(a) Features mined with the input image

The features mined with input images J_r are LGBP and LDTP. These features are mined by dividing the images into regions of interest and classifying those regions.

(i) LGBP

The basic idea of LGBP [28] is that the LBP operator is adapted on the Gabor input images instead of adapting LBP on raw images. From each Gabor image we can consider the characteristic of the LBP histogram. By modifying histogram features on the entire energy images LGBP characteristic is produced. So, the LGBP operator feature size is large when compared to LBP, which owes to Gabor decomposition. An actual LBP operator plots image pixels with thresholding of 3×3 nearest pixel $\lambda_p(p = 0, 1, ..., 7)$ using mid-value $\lambda_c$and a binary number is chosen as an output. The value of threshold using an image is binary form and is given below,

$$\Re\left(\lambda_p - \lambda_c\right) = \begin{cases} 1, & \lambda_p \geq \lambda_c \\ 0, & \lambda_p < \lambda_c \end{cases} \tag{11}$$

After that, the LBP pattern pixel is given as,

$$LBP = \sum_{p=0}^{7} \Re\left(\lambda_p - \lambda_c\right) 2^p \tag{12}$$

The feature LGBP is termed as C_1.

(i) LDTP

The LDTP [29] helps to encode the texture of the image by evaluating the edge response with eight directions considering the second derivative Gaussian mask and is given by,

$$\mu = \frac{1}{9}\left(\tau_c + \sum_{p=0}^{7} \tau_p\right) \tag{13}$$

Where, $\tau_c$is a central pixel, and $\tau_p$is the peripheral pixel.

To produce LDTP code, the indicator is defined, which is given as,

$$\vartheta(x, y) = \begin{cases} +1 & If\ x >= 0\ \ and\ \ y >= 0 \\ -1 & If\ x <= 0\ \ and\ \ y <= 0 \\ 0 & Otherwise \end{cases} \tag{14}$$

Where, x and y represent variants of LDTP.

(a) Features mined with optic disc and blood cells

The extracted optic discs and blood cells segment from the preprocessed image Q, and the features, like entropy, variance, standard deviation, skewness, energy, kurtosis, and mean, are computed.

(i) Mean

It is calculated by the image containing the average of the pixels and is given by,

$$A_2 = \frac{1}{|d(C_z)|} \times \sum_{z=1}^{|d(C_z)|} d(C_z) \tag{15}$$

where, z symbolize complete segments, $d(C_z)$ signifies pixel value at each segment, and $|d(C_z)|$ express total pixel in the segment. The feature mean is given in A_2.

(i) Variance

The value of the mean variance is computed and is given by,

$$A_3 = \frac{\sum_{z=1}^{|d(C_z)|} |C_z - A_2|}{d(C_z)} \tag{16}$$

Where, $C_z$represents total pixels and A_2signifies mean. The variance feature is given in A_3.

(i) Energy

The energy contained in each segment is computed by adding energies of pixel contained in each segment and is expressed as,

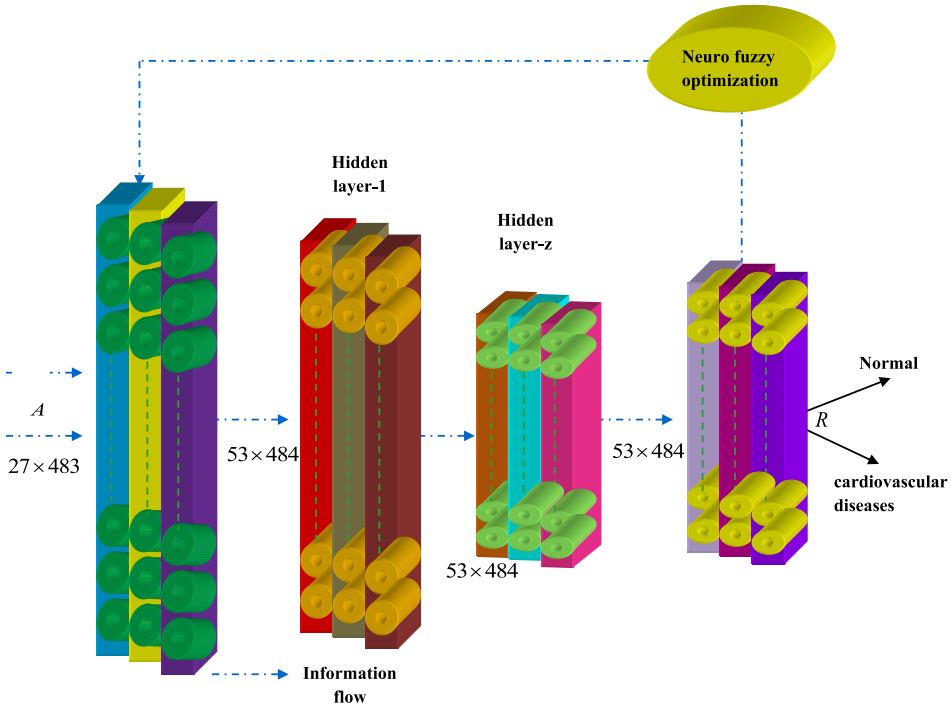

Fig. 2. Structure of DNFN.

$$A_4 = \sum_{z=1}^{|d(C_z)|} \psi(C_z) \tag{17}$$

In addition, the energy is given in A_4.

(i) Kurtosis

Kurtosis A_5 symbolizes the peak's sharpness using a frequency-distribution curve, and it is used to describe the degree wherein the scores cluster.

(i) Entropy

The entropy [16] symbolizes a metric utilized to discover uncertainty. The entropy is given by,

$$A_5 = -C\log(C) \tag{18}$$

where,C signifies distribution of pixels probability and the feature entropy is provided by A_5.

(i) Skewness

Based on a numerical value it describes object shape and is expressed as A_6

(i) Standard deviation

It describes variance square root and is given in A_7.

The feature vector is given by concatenating the features generated from each segment and is expressed as,

$$A = \{A_1, A_2, A_3, A_4, A_5, A_6, A_7\} \tag{19}$$

Where, A_1 express mean A_2 signifies variance, A_3 is energy feature, A_4 refers to kurtosis feature, A_5 represent entropy feature, and A_6 express skewness feature and A_7 is the standard deviation.

3.6. Prediction of cardiovascular diseases using proposed FC—HOA-based DNFN

This section describes the DNFN [25] used to predict cardiovascular diseases. DNFN is adapted as a widespread approximator as its easy structure utilizes modern activation functions. The DNFN is used to handle a huge number of images. It contains the capability to address a large count of optimization problems. It provides better and prevents over fitting problems, which is adapted as an effective classifier as of its small model. Also, it discards the problems given by the classical activation function design, which is also simple and reliable to train the effectual performance. Finally, the feature vector$A$is subjected to DNFN to predict CVD.

(a) Structure of DNFN

In DNFN [25], two steps are performed wherein the initial one is executed with a deep neural network, and the second is done with fuzzy logic to compute the system objective. It comprises the input and hidden layer for verifying and learning, and the output layer. The structure is modeled in Fig. 2.

To describe data processing the mapping of each output and input is performed. Assume two given values z and a only use consequenty, the equation is,

$$\mathrm{X}_{1,w}(z) = f\,C_w(z) \text{ or } \mathrm{X}_{1,w} = f\,\mathrm{P}_{w-2}(a), \quad \forall w = 1,2,3 \tag{20}$$

Where, a and z is input to all wth entities, fC_w $f\mathrm{P}_{w-2}$ indicates antecedent membership function, and $\mathrm{X}_{1,w}$ is membership degree function. The equation is,

$$f\,C_w(z) = \frac{1}{1 + \left|\frac{z - D_w}{N_w}\right|^{2R_w}} \tag{21}$$

Where, R_w, D_w and N_w refers to membership function. The firing strength of the rule implies the membership variable is,

$$\mathrm{X}_{2,w} = \mu_w = f\,C_w(z) f\,\mathrm{P}_{w-2}(a)\ , \forall w = 1,2 \tag{22}$$

Likewise, normalization in layer 3, wherein the proportion of firing strength of *w*th is the rule which is evaluated by each entity and μ_w is the general network attribute. Thus, firing strength normalized the result of each rule and is given,

$$X_{3,w} = \overline{\mu}_w = \frac{\mu_w}{\mu_1 + \mu_2} \ , \ \forall w = 1,2 \tag{23}$$

Furthermore, the defuzzification layer is also known as fourth layer, wherein each consequent is evaluated to indicate output and is given by,

$$X_{4,w} = \overline{\mu}_w I_w = \overline{\mu}_w (E_w z + F_w a + C_w) \ , \ \forall w = 1,2 \tag{24}$$

where, *E, F* and *C* is a set of parameters. The final result computation is given,

$$X_{5,w} = \sum_w \overline{\mu}_w I_w = \frac{\sum_w \mu_w I_w}{\sum_w \mu_w} \tag{25}$$

Thus, *R* is denoted as the output generated from DNFN, which helps detect if the image is normal or Hypertension.

(a) DNFN Training with proposed FC—HOA

FC—HOA is created by combining FC and HOA which performs the DNFN training. The HOA [27] is motivated by Particle Swarm Optimization (PSO) and is devised in a particle that updates position with learning, which provides a tradeoff between exploration and exploitation. Meanwhile, FC [26] is acquired by averaging some consecutive observations wherein the values are weighed so that recent observations present a high issue on average. Next, there is no need to maintaining the dataset of all numbers. To determine small shifts FC is utilized to handle value of the target. The FC enhanced complete process quality and devised using historical observations. The integration of FC and HOA improves the complete efficiency and provides an optimum solution. Steps of the proposed FC—HOA are given:

Step 1: **Initialization**

Solution initialization is the first step which is given as *T* with total εsolution (i.e.)$1 \le \nu \le \varepsilon$

$$T = \{T_1, T_2, \ldots, T_\nu, \ldots, T_\varepsilon\} \tag{26}$$

Where, ε refers to a total solution and T_ν its νth solution.

Step 2: **Error determination**

Minimization issue is done because the solution is discovered with error and Hence, best solution creating minimal Mean Square Error (MSE) given by,

$$MS_{err} = \frac{1}{g} \sum_{h=1}^{g} [M_h - R]^2 \tag{27}$$

Where, M_h refers output and *R* refers output created from DNFN, *g* no of data samples wherein $1 < h \le g$.

Step 3: **Movement evaluation applied to horse**

To obtain a global optimum solution with improved accuracy we have to use HOA. As per HOA [27], the movement employed on a horse in every iteration is expressed as,

$$T_d^{iter,age} = I_d^{iter,age} + T_d^{(Iter-1),Age} \tag{28}$$

Where, $T_d^{Iter,age}$ is horse position, is present iteration, and is the velocity of the horse.

The motion of horses is given as,

$$\overrightarrow{I}_d^{iter,\alpha} = U_d^{Iter,\alpha} + V_d^{Iter,\alpha} \tag{29}$$

$$\overrightarrow{I}_d^{iter,\beta} = U_d^{Iter,\beta} + W_d^{Iter,\beta} + Y_d^{iter,\beta} + V_d^{iter,\beta} \tag{30}$$

$$\overrightarrow{I}_d^{iter,\gamma} = U_d^{Iter,\gamma} + W_d^{Iter,\gamma} + Y_d^{iter,\gamma} + Z_d^{iter,\gamma} + V_d^{iter,\gamma} + O_d^{iter,\gamma} \tag{31}$$

$$\overrightarrow{I}_d^{iter,\delta} = U_d^{Iter,\delta,} + Z_d^{Iter,\delta} + O_d^{iter,\delta} \tag{32}$$

Thus, the equation can be rewritten as,

$$T_d^{age}(\upsilon+1) = \overrightarrow{I}_d^{age}(\upsilon+1) + \overrightarrow{T}_d^{age} \tag{33}$$

$$T_d^{age}(\upsilon+1) - \overrightarrow{T}_d^{age} = \overrightarrow{I}_d^{age}(\upsilon+1) \tag{34}$$

Apply FC [26],

$$D^\alpha[T_d^{age}(\upsilon+1)] = \overrightarrow{I}_d^{age}(\upsilon+1) \tag{35}$$

Where, α symbolize fractional coefficient.

$$\begin{aligned} T_d^{age}(\upsilon+1) - \alpha T_d^{age}(\upsilon) - \frac{1}{2}\alpha.T_d^{age}(\upsilon-1) - \frac{1}{6}(1-\alpha).T_d^{age}(\upsilon-2) \\ - \frac{1}{24}\alpha(1-\alpha)(2-\alpha).T_d^{age}(\upsilon-3) \\ = I_d^{age}(t+1) \end{aligned} \tag{36}$$

Assume$age = \alpha$,

$$I_d^{iter,\alpha} = U_d^{\alpha} + V_d^{iter,\alpha} \tag{37}$$

$$I_d^{iter,age}(\upsilon+1) = U_d^{\alpha}(\upsilon+1) + V_d^{\alpha}(\upsilon+1) \tag{38}$$

Projected FC—HOA updation is expressed as,

$$\begin{aligned} T_d^{age}(\upsilon+1) = \alpha T_d^{age}(\upsilon) + \frac{1}{2}\alpha.T_d^{age}(\upsilon-1) + \frac{1}{6}(1-\alpha).T_d^{age}(\upsilon-2) \\ + \frac{1}{24}\alpha(1-\alpha)(2-\alpha).T_d^{age}(\upsilon-3) + U_d^{\alpha}(\upsilon+1) + V_d^{\alpha}(\upsilon+1) \end{aligned} \tag{39}$$

Step 4: **Grazing evaluation**

The abrasion area is modeled through each horse using coefficient g in such a way that each horse grazes on specific areas and is formulated as,

$$U_d^{Iter,age} = c_{iter}(\tau + \rho\kappa)\left[T_d^{(iter-1)}\right] \tag{40}$$

Where, $U_d^{iter,age}$ shows motion parameter of the horse and $\omega_g$is linearity, τsignifies upper bound, ρ signifies random number and κis lower bound.

$$c_d^{iter,age} = c_d^{(iter-1),age} \times \omega_g \tag{41}$$

Step 5: **Hierarchy evaluation**

By following a leader the horses pass their lives and are taken by human beings which is given,

$$W_d^{iter,age} = w_d^{iter,age}\left[T_*^{(iter-1)} - T_d^{(iter-1)}\right] \tag{42}$$

Where, $W_d^{iter,age}$ is the effort of best horse location, and $T_*^{(iter-1)}$ is the location of the best horse, ϖ is a factor, and $\omega_d^{(iter-1),age}$ which means to follow the strong person which is tendency of herd horse.

$$w_d^{iter,age} = w_d^{(iter-1),age} \times \varpi \tag{43}$$

Step 6: **Sociability evaluation**

For average horse position, sociability evaluation is a movement and is given by,

$$Y_d^{iter,age} = y_d^{iter,age}\left[\left(\frac{1}{\upsilon}\sum_{l=1}^{\upsilon} T_l^{(iter-1)}\right) - T_d^{(iter-1)}\right] \tag{44}$$

$$y_d^{iter,age} = y_d^{(iter-1),age} \times \varpi_y \tag{45}$$

Where, $Y_d^{iter,age}$ shows the social motion of the horse, and $y_d^{iter,age}$ shows concerned horse orientation, ϖ_y refers to the weight factor.

Step 7: **Imitation evaluation**

Table 1
Algorithm of devised FC—HOA.

```
Input: Solution T
Output: The best solution T*
Begin:
using Eq. (27) error evaluation;
While not satisfied stopping criterion acquires, do
  Compute ages α, β, γ, δ
  Calculate the velocity of each horse using Eqs. (29)–(32)
  Discover a new position with grazing using Eq. (40)
  Discover new position with Hierarchy using Eq. (42)
  Discover a new position with sociability using Eq. (44)
  Discover a new position with imitation using Eq. (46)
  Discover a new position with a defence mechanism using Eq. (48)
  Discover a new position with roaming using Eq. (50)
End while;
using Eq. (27), revaluate error;
υ = υ + 1;
End
```

For determining the suitable pasture location horses copy each other which is given by,

$$Z_d^{iter,age} = z_d^{iter,age}\left[\left(\frac{1}{my}\sum_{l=1}^{my} T_l^{(iter-1)}\right) - T^{(iter-1)}\right] \tag{46}$$

$$z_d^{iter,age} = z_d^{(iter-1),age} \times \varpi \tag{47}$$

Where, $Z_d^{iter,age}$ motion vector of the horse moving to the best horse's average *my* the best location of several horses, and $\varpi$is per cycle reduction factor, and $z_d^{(iter-1),age}$ is concerned horse behavior.

Step 8: **Defense mechanism evaluation**

Model horses away from unsuitable positions is corresponding to the defense mechanism and is given,

$$V_d^{iter,age} = -v_d^{iter,age}\left[\left(\frac{1}{qN}\sum_{l=1}^{qN} V_l^{(iter-1)}\right) - V^{(iter-1)}\right] \tag{48}$$

$$v_d^{iter,age} = v_d^{(iter-1),age} \times \varpi \tag{49}$$

Step 9: **Evaluation of room**

Younger ages we were determined to ride the horses, which means mitigates after maturity, which is given,

$$O_d^{iter,age} = o_d^{iter,age}\rho T^{(iter-1)} \tag{50}$$

Where, $O_d^{iter,age}$ is random velocity

$$o_d^{iter,age} = o_d^{(iter-1),age} \times \varpi \tag{51}$$

Step 10: **Error computation to update solutions**

Weights associated with the least error are employed to train DNFN where the error of the new solution is computed.

Step 11 **Terminate**

The highest iteration is acquired so we have to produce optimal weights until it acquired. Table 1 shows the algorithm of the created FC—HOA.

The output generated with FC—HOA-based DNFN is expressed by *R* either normal or Hypertension.

4. Results and discussion

Using specificity, sensitivity and accuracy the efficiency of FC—HOA-based DNFN is evaluated by altering training data and K-fold.

4.1. Experimental setup

The experimentation is performed on PC with Windows 10 OS, 2GB RAM, and Intel core processor. The implementation tool used here is Python.

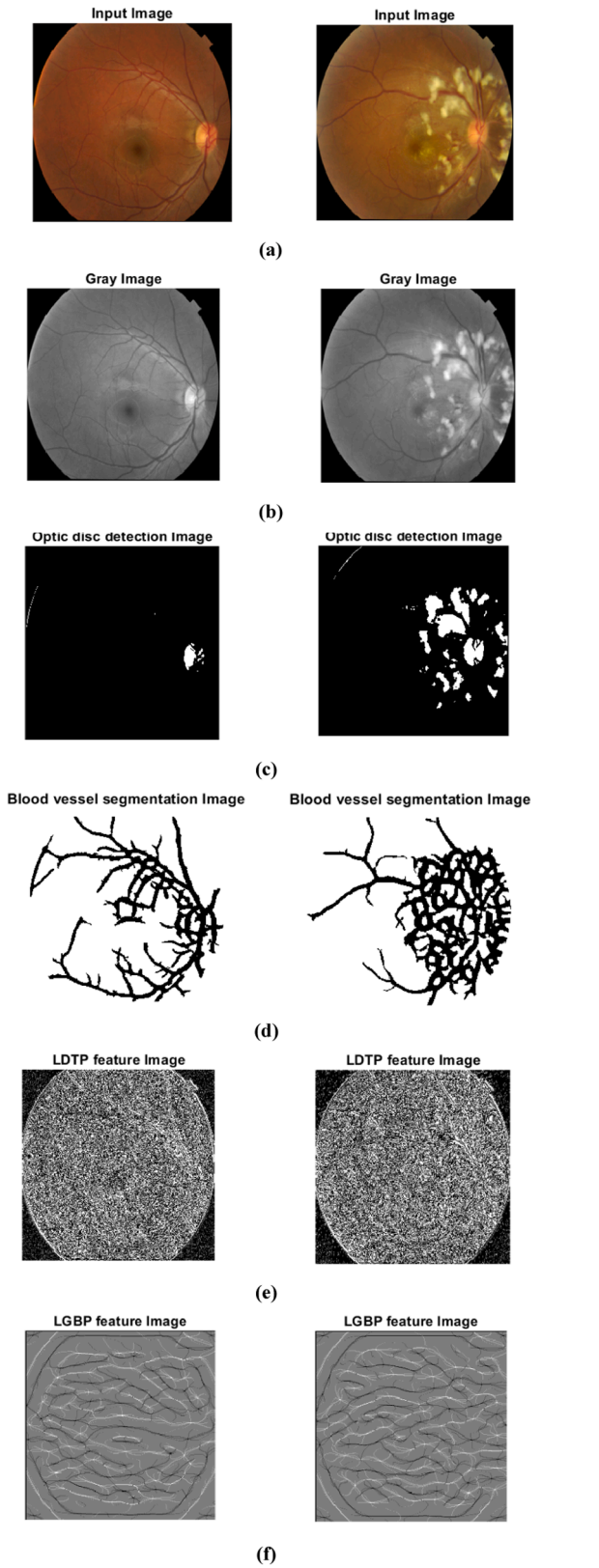

Fig. 3. Experimental outcomes of projected FC—HOA-based DNFN (a) Input image (b) Grayscale image (c) Optic disc image (d) Blood vessel image (e, f) LDTP image LGBP image.

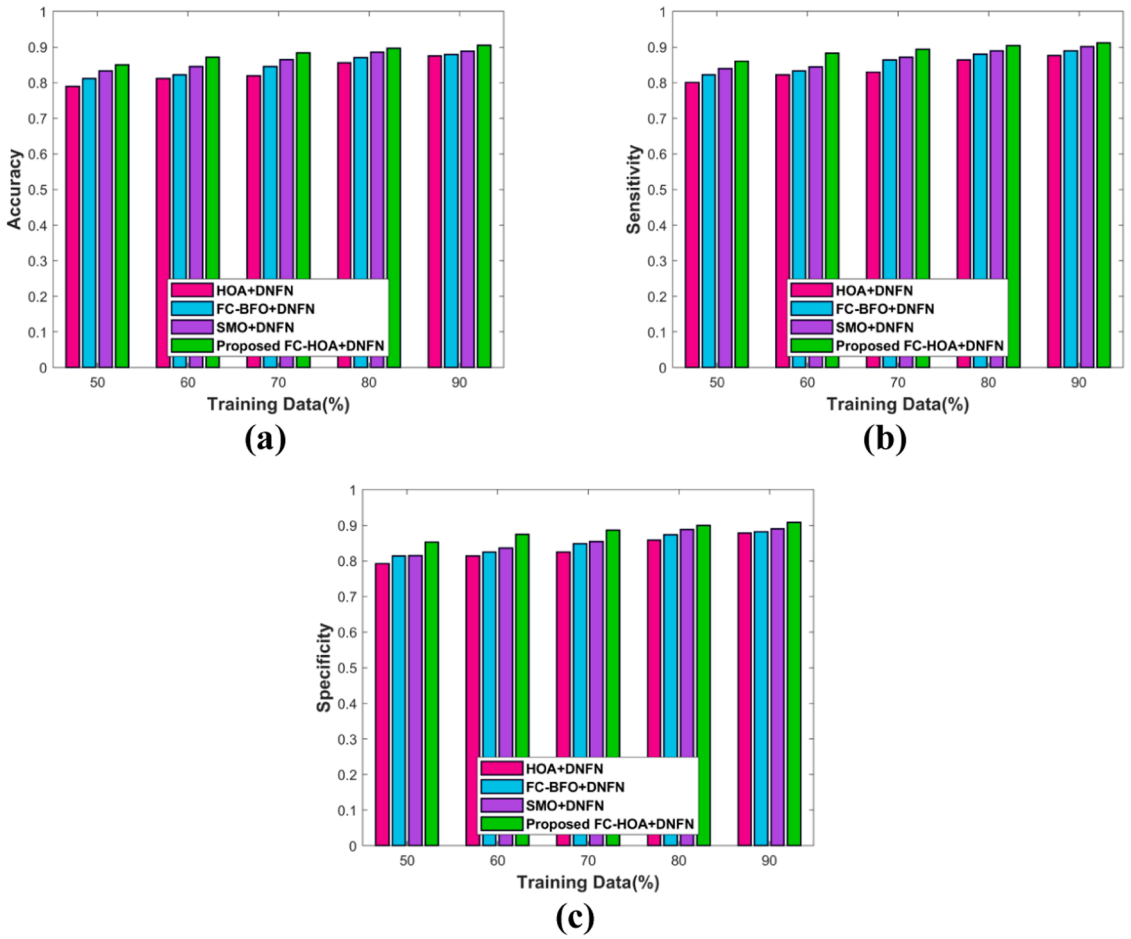

Fig. 4. Evaluation by changing training data (a) Accuracy (b) Sensitivity (c) Specificity.

4.2. Dataset used

The experimentation is performed using 1000 fundus images having 39 categories [22]. First, we define the process of fundus imaging is obtaining a two-dimensional (2D) representation of the 3D by using reflected light and retinal tissues, which are semitransparent viewed into the imaging plane. Here are thousand fundus images that belong to thirty nine classes. These images comprise 209,494 fundus images for training, validating and testing deep learning infrastructure. In this dataset, the image copyright fits in JSIEC.

4.3. Experimental outcomes

Fig. 3 represents the experimental results of the projected method. Fig. 3a and b shows the set of input images is revealed and reveals the grayscale image. Similarly, Fig. 3c and d displays the optical disc image and depicts the blood vessel image. Fig. 3e and f displays the LDTP image and the LGBP image.

4.4. Evaluation measures

The achievement of our approach is evaluated on the basis of the performance metrics, namely accuracy, sensitivity, and specificity.

Accuracy: It defines the proportion of the addition of true positive rate (TPR) + true negative rate (TNR) and the addition of true positive rate (TPR) + False Negative Rate (FNR).+True Negative Rate(TNR) + False Positive Rate (FPR).

$$Accuracy\ a = \frac{(P+Q)}{(P+V+Q+S)} \tag{52}$$

where, P indicates the TPR, S indicates the FNR, V indicates the FPR, and Q indicates the TNR

Sensitivity: It indicates the capability of a method to properly classify the patients with cardiovascular disease. The equation of sensitivity is given below,

$$\lambda = \frac{c}{c+e} \tag{53}$$

Specificity: It expresses the aptitude of a method to properly identify people without the disease. The specificity is computed by below equation,

$$\gamma = \frac{o}{o+p} \tag{54}$$

4.5. Algorithm analysis

Using specificity, accuracy and sensitivity the evaluations strategies are defined by varying training data and K-fold method.

4.5.1. Evaluation training data

Fig. 4 reveals Evaluation by varying training data. Fig. 4a indicates For 50% data, the accuracy generated by HQA+DNFN is 0.789, FC+BFO+DNFN is 0.811, SMO+DNFN is 0.834, and projected FC—HOA-based DNFN is 0.850. and, for 90% data, the accuracy created by HQA+DNFN is 0.876, FC+BFO+DNFN is 0.879, SMO+DNFN is 0.888, and proposed FC—HOA-based DNFN is 0.905. The performance

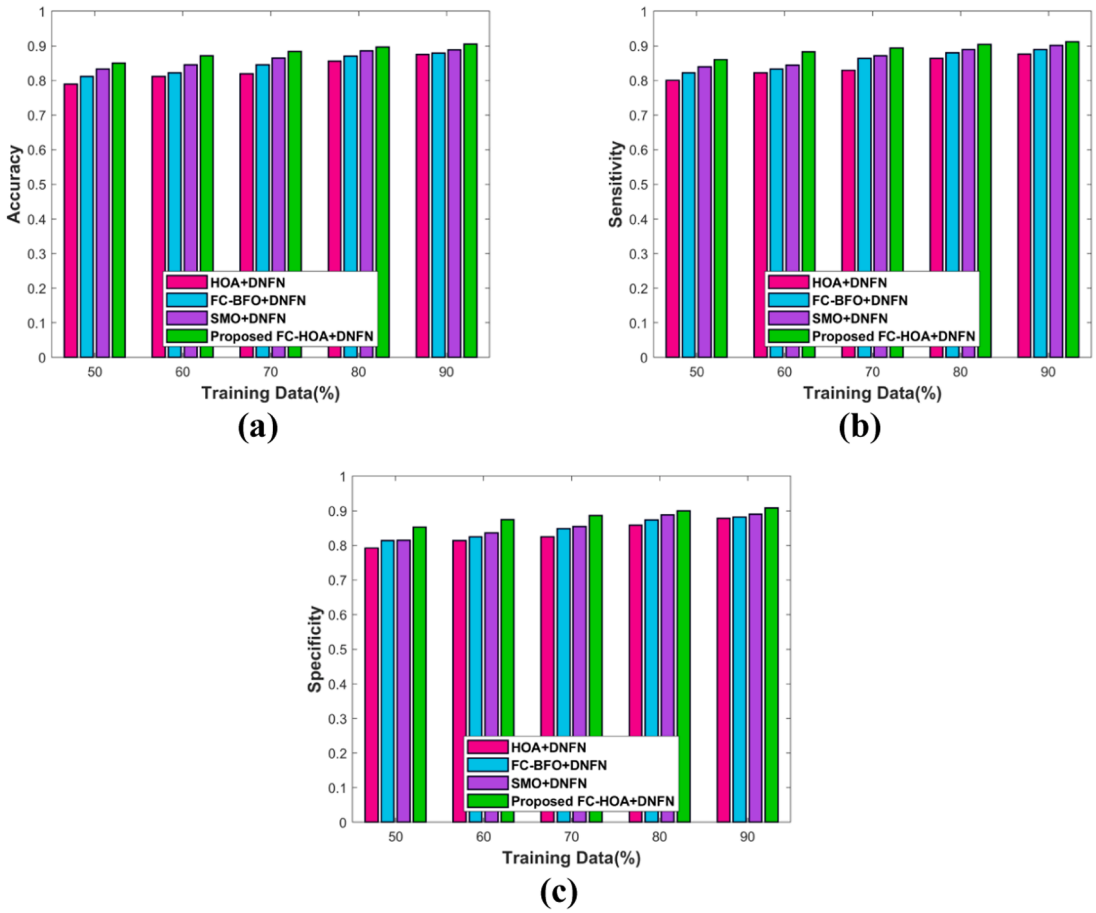

Fig. 5. Evaluation of projected FC—HOA-based DNFN by varying K-fold (a) Accuracy (b) Sensitivity (c) Specificity.

improvement of HQA+DNFN, FC+BFO+DNFN, and SMO+DNFN concerning proposed FC—HOA-based DNFN using accuracy is 3.204, 2.872, 1.878%. Fig. 4b indicates for 50% data, the sensitivity created by HQA+DNFN is 0.800, FC+BFO+DNFN is 0.823, SMO+DNFN is 0.840, and projected FC—HOA-based DNFN is 0.861. Also, for 90% data the sensitivity created by HQA+DNFN is 0.876, FC+BFO+DNFN is 0.889, SMO+DNFN is 0.901, and projected FC—HOA-based DNFN is 0.912. The performance improvement of HQA+DNFN, FC+BFO+DNFN, and SMO+DNFN concerning projected FC—HOA-based DNFN using sensitivity is 3.947, 2.521, 1.206%. Fig. 4c indicates for 50% data, the specificity generated by HQA+DNFN is 0.792, FC+BFO+DNFN is 0.814, SMO+DNFN is 0.815, and projected FC—HOA-based DNFN is 0.853. Also, for 90% data the specificity generated by HQA+DNFN is 0.878, FC+BFO+DNFN is 0.882, SMO+DNFN is 0.891, and projected FC—HOA-based DNFN is 0.908. The performance improvement of HQA+DNFN, FC+BFO+DNFN, and SMO+DNFN concerning projected FC—HOA-based DNFN using specificity is 3.303, 2.863, 1.872%.

4.5.2. Evaluation with K-fold

Fig. 5 displays the Evaluation of the projected FC—HOA-based DNFN by varying the K-fold. Fig. 5a indicates for k-fold = 5, 0.857 high accuracy is created by projected FC—HOA-based DNFN, whereas the accuracy achieved by HQA+DNFN, FC+BFO+DNFN, SMO+DNFN are 0.797, 0.819, 0.841. Also, for k-fold = 9, 0.910 high accuracy is created by the projected FC—HOA-based DNFN, whereas the accuracy achieved by HQA+DNFN, FC+BFO+DNFN, SMO+DNFN are 0.883, 0.887, 0.896. The achievement of HQA+DNFN, FC+BFO+DNFN, and SMO+DNFN concerning projected FC—HOA-based DNFN using accuracy is 2.967, 2.527, 1.538%. Fig. 5b indicates for k-fold = 5, 0.868 high sensitivity is created by projected FC—HOA-based DNFN while the sensitivity achieved by HQA+DNFN, FC+BFO+DNFN, SMO+DNFN are 0.808, 0.830, 0.852. Also, for k-fold = 9, 0.919 highest sensitivity is created by projected FC—HOA-based DNFN, whereas the sensitivity achieved by HQA+DNFN, FC+BFO+DNFN, SMO+DNFN are 0.884, 0.897, 0.909. The achievement of HQA+DNFN, FC+BFO+DNFN, and SMO+DNFN concerning projected FC—HOA-based DNFN using sensitivity is 3.808, 2.393, 1.088%. Fig. 5c indicates for k-fold = 5, 0.861 high specificity is created by projected FC—HOA-based DNFN, whereas the specificity achieved by HQA+DNFN, FC+BFO+DNFN, SMO+DNFN are 0.800, 0.822, 0.844. And, for k-fold = 9, 0.915 highest specificity is created by projected FC—HOA-based DNFN, whereas the specificity achieved by HQA+DNFN, FC+BFO+DNFN, SMO+DNFN are 0.886, 0.890, 0.899. The achievement of HQA+DNFN, FC+BFO+DNFN, and SMO+DNFN concerning projected FC—HOA-based DNFN using specificity is 3.169, 2.732, 1.748%.

4.6. Comparative strategies

The strategies taken for the evaluation includes DNN [10], DRN [6], CNN [20], Multi-task LSTM [21], IDM_IDSS [7], MaLCaDD [8], and projected FC—HOA+DNFN.

4.7. Comparative analysis

Differing training data and K-fold define the evaluations of strategies.

4.7.1. Evaluation with training data

Fig. 6 shows evaluation by varying training data. Fig. 6a indicates the accuracy of the methods. For 50% data, the accuracy achieved by DNN is

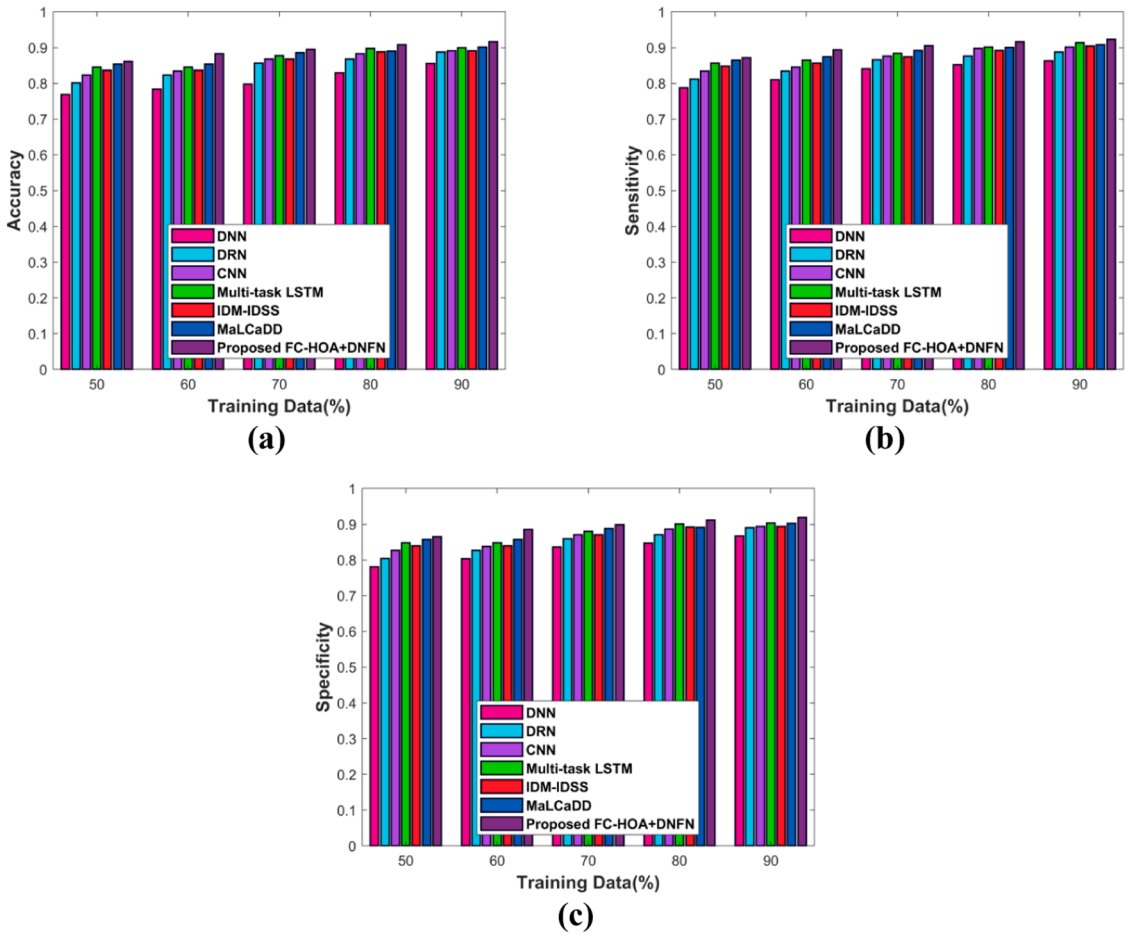

Fig. 6. Evaluation methods by varying training data (a) Accuracy, (b) Sensitivity, (c) Specificity.

0.769, DRN is 0.801, CNN is 0.823, Multi_taskLSTM is 0.846, IDM_IDSS is 0.837, MaLCaDD is 0.854 and Projected FC_HOA_DNFN is 0.862. Also, for 90% data, the accuracy achieved by DNN is 0856, DRN is 0.888, CNN is 0.891, Multi_taskLSTM is 0.900, IDM_IDSS is 0.891, MaLCaDD is 0.902, and projected FC_HOA_DNFN is 0.916. The achievement of projected FC—HOA + DNFN with the comparative methods, such as DNN, DRN, CNN, Multi-task LSTM, IDM_IDSS, MaLCaDD is 6.550, 3.056, 2.729, 1.746, 2.729 and 1.528%. Fig. 6b indicates sensitivity of the methods. For 60% data, the sensitivity achieved by DNN is 0.81, DRN is 0.835, CNN is 0.846, Multi_taskLSTM is 0.865, IDM_IDSS is 0.857, MaLCaDD is 0.874 and Projected FC_HOA_DNFN is 0.894. Also, for 90% data, the sensitivity achieved by DNN is 0.853, DRN is 0.888, CNN is 0.901, Multi_taskLSTMis 0.913, IDM_IDSS is 0.904, MaLCaDD is 0.908 and Projected FC_HOA_DNFN is 0.923. Fig. 6c indicates specificity of the comparative methods. For 70% data, the specificity achieved by DNN, DRN, CNN, Multi_taskLSTM, IDM_IDSS, MaLCaDD, and Projected FC_HOA_DNFN are 0.836, 0.860, 0.871, 0.880, 0.871, 0.889 and 0.898.

4.7.2. Evaluation with K-fold

Fig. 7 shows evaluation using K-fold validation. Fig. 7a indicates the accuracy plot of the methods. For K-fold = 5, accuracy achieved by DNN, DRN, CNN, Multi_taskLSTM, IDM_IDSS, MaLCaDD and Projected FC_HOA_DNFN are 0.793, 0.769, 0.816, 0.838, 0.829, 0.807 and0.842. Also, for K-fold = 9, the accuracy achieved by DNN, DRN, CNN, Multi_taskLSTM, IDM_IDSS, MaLCaDD and Projected FC_HOA_DNFN are 0.878, 0.837, 0.881, 0.890, 0.881, 0.899 and 0.911. Fig. 7b indicates the sensitivity plot of the methods. For K-fold = 5, sensitivity achieved by DNN, DRN, CNN, Multi_taskLSTM, IDM_IDSS, MaLCaDD and Projected FC_HOA_DNFN are 0.793, 0.769, 0.816, 0.838, 0.829, 0.807, and 0.842. Also, for K-fold = 9, the sensitivity achieved by DNN, DRN, CNN, Multi_taskLSTM, IDM_IDSS, MaLCaDD and Projected FC_HOA_DNFN are 0.869, 0.845, 0.882, 0.894, 0.885, 0.890 and0.899. Fig. 7c indicates the specificity plot of the methods. For K-fold = 5, the specificity achieved by DNN, DRN, CNN, Multi_taskLSTM, IDM_IDSS, MaLCaDD and Projected FC_HOA_DNFN are 0.803, 0.772, 0.825, 0.848, 0.839, 0.826 and0.852. and for K-fold = 9, the specificity achieved by DNN, DRN, CNN, Multi_taskLSTM, IDM_IDSS, MaLCaDD and Projected FC_HOA_DNFN are 0.890, 0.859, 0.893, 0.902, 0.893, 0.901 and 0.913.

4.8. Comparative discussion

Table 2 represents the evaluation with K-fold method and training data. When the analysis performed by varying the training data, the methods like DNN, DRN, CNN, Multi_taskLSTM, IDM_IDSS, MaLCaDD and Projected FC_HOA_DNFN have the accuracy of 0.856, 0.888, 0.891, 0.900, 0.891, 0.902 and 0.916, respectively. Similarly, by varying the k-fold values, the accuracy obtained for Projected FC_HOA_DNFN is 0.911. When the analysis performed by varying the training data, the methods like DNN, DRN, CNN, Multi_taskLSTM, IDM_IDSS, MaLCaDD and Projected FC_HOA_DNFN have the sensitivity of 0.863, 0.888, 0.901, 0.913, 0.904, 0.908 and 0.923. Whereas, by varying the k-fold values, the sensitivity obtained for Projected FC_HOA_DNFN is 0.899. When the analysis performed by varying the training data, the methods like of DNN, DRN, CNN, Multi_taskLSTM, IDM_IDSS, MaLCaDD and Projected FC_HOA_DNFN have the specificity of 0.867, 0.891, 0.894, 0.903, 0.894, 0.902, and 0.919. Whereas, by varying the k-fold values, the specificity obtained for Projected FC_HOA_DNFN is 0.913.

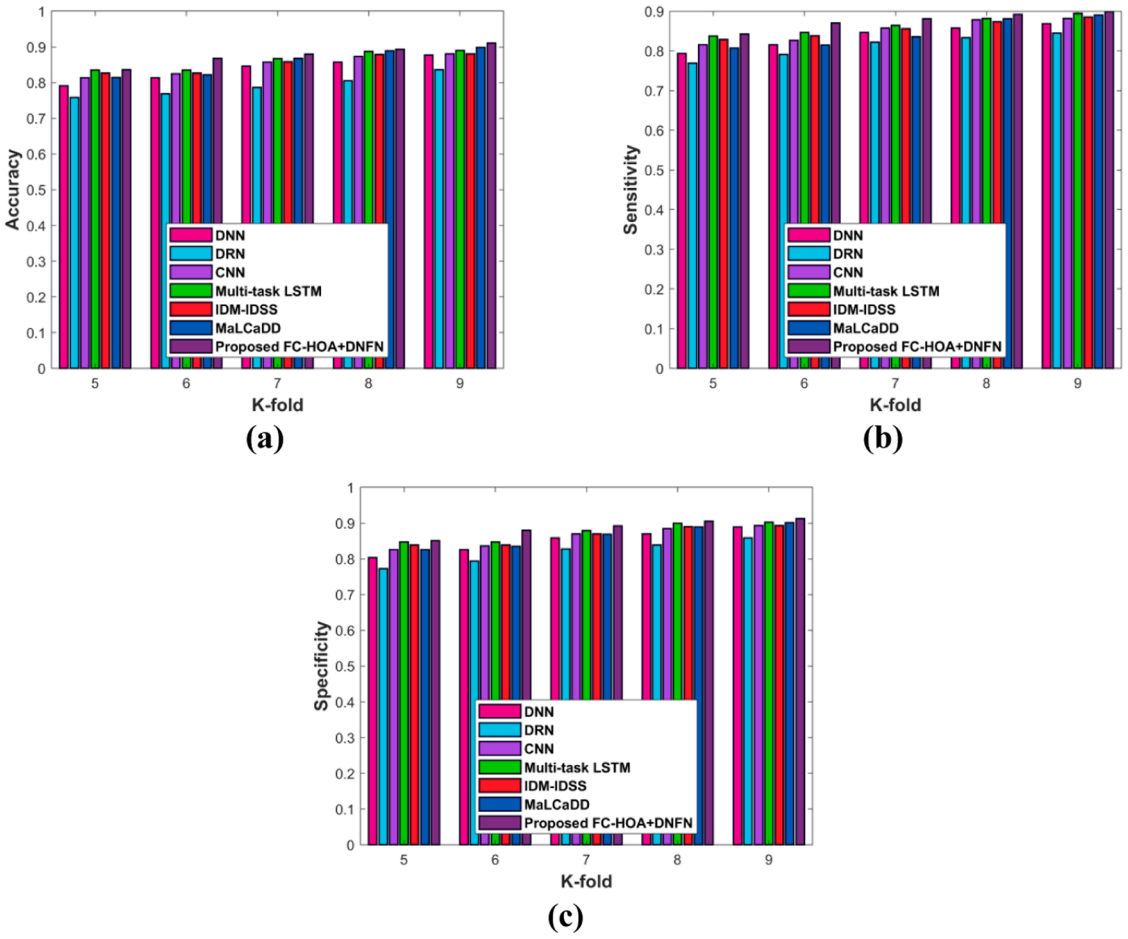

Fig. 7. Evaluation methods by varying K-fold (a) Accuracy (b) Sensitivity (c) Specificity.

Table 2
Comparative evaluation.

Variation	Training data			K-fold		
Metrics	Accuracy	Sensitivity	Specificity	Accuracy	Sensitivity	Specificity
DNN	0.856	0.863	0.867	0.878	0.869	0.890
DRN	0.888	0.888	0.891	0.837	0.845	0.859
CNN	0.891	0.901	0.894	0.881	0.882	0.893
Multi-task LSTM	0.900	0.913	0.903	0.890	0.894	0.902
IDM_IDSS	0.891	0.904	0.894	0.881	0.885	0.893
MaLCaDD	0.902	0.908	0.902	0.899	0.890	0.901
Proposed FC—HOA+DNFN	**0.916**	**0.923**	**0.898**	**0.911**	**0.899**	**0.913**

5. Conclusion

This paper devises productive model for CVD risk prediction using the retinal fundus images, which are subjected to pre-processing with grayscale conversion to make them suitable for improved processing. Then, discovery of the optic disc is made with binarization and circle fixing. Next, the blood vessel segmentation is done with deep joint segmentation, wherein the dice coefficient and binary cross-entropy are integrated to evaluate the distance. Next, mining effectual features are done to mine suitable features that include statistical features. Meanwhile, the features are extracted with the input image, like LDTP and LGBP. Finally, the prediction of cardiovascular risk is performed with DNFN such that the risks are categorized into normal and hypertensive. Here, the DNFN is trained with newly developed FC—HOA and is acquired by joining FC and HOA. As a result, the projected FC—HOA-based DNFN provide high performance with the highest of 91.6% accuracy, 92.3% sensitivity, and 91.9% specificity. Future works include considering other advanced database to check the efficiency of the projected model.

Declaration of Competing Interest

The authors declare no conflict of interest.

References

[1] Cheung CY, Tay WT, Mitchell P, Wang JJ, Hsu W, Lee ML, Lau QP, Zhu AL, Klein R, Saw SM, Wong TY. Quantitative and qualitative retinal microvascular characteristics and blood pressure. J Hypertens 2011;29(7):1380–91.
[2] Wong TY, Hubbard LD, Klein R, Marino EK, Kronmal R, Sharrett AR, Siscovick DS, Burke G, Tielsch JM. Retinal microvascular abnormalities and blood pressure in older people: the cardiovascular health study. Br J Ophthalmol 2002;86(9):1007–13.
[3] Hubbard LD, Brothers RJ, King WN, Clegg LX, Klein R, Cooper LS, Sharrett AR, Davis MD, Cai J, Atherosclerosis Risk in Communities Study Group. Methods for

evaluation of retinal microvascular abnormalities associated with hypertension/sclerosis in the atherosclerosis risk in communities study. Ophthalmology 1999;106(12):2269–80.
[4] Wang JJ, Mitchell P, Leung H, Rochtchina E, Wong TY, Klein R. Hypertensive retinal vessel wall signs in a general older population: the blue mountains eye study. Hypertension 2003;42(4):534–41.
[5] Yu T, Mitchell P, Berry G, Li W, Wang JJ. Retinopathy in older persons without diabetes and its relationship to hypertension. Arch Ophthalmol 1998;116(1):83–9.
[6] G. Dai, C. Zhang, and W. He, "Screening of diabetes and hypertension based on retinal fundus photographs using deep learning", medRxiv, 2019.
[7] Mahiddin NB, Othman ZA, Bakar AA, Arzuar N, Rahim A. An interrelated decision-making model for an intelligent decision support system in healthcare. IEEE Access 2022;10:31660–76.
[8] Rahim A, Rasheed Y, Azam F, Anwar MW, Rahim M. An integrated machine learning framework for effective prediction of cardiovascular diseases. IEEE Access 2021;9:106575–88.
[9] Poplin R, Varadarajan AV, Blumer K, Liu Y, McConnell MV, Corrado GS, Peng L, Webster DR. Prediction of cardiovascular risk factors from retinal fundus photographs via deep learning. Nat Biomed Eng 2018;2(3):158–64.
[10] Ting DSW, Peng L, Varadarajan AV, Liu TYA. Novel retinal imaging in evaluation of cardiovascular risk factors and systemic vascular diseases. Diabetic retinopathy and cardiovascular disease, 27. Karger Publishers; 2019. p. 106–18.
[11] Taylor AM, MacGillivray TJ, Henderson RD, Ilzina L, Dhillon B, Starr JM, Deary IJ. Retinal vascular fractal dimension, childhood IQ, and cognitive ability in old age: the Lothian birth cohort study 1936. PLoS One 2015;10(3):e0121119.
[12] McGrory S, Taylor AM, Kirin M, Corley J, Pattie A, Cox SR, Dhillon B, Wardlaw JM, Doubal FN, Starr JM, Trucco E, MacGillivray TJ, Deary IJ. Retinal microvascular network geometry and cognitive abilities in community-dwelling older people: the Lothian birth cohort 1936 study. Br J Ophthalmol 2017;101(7):993–8.
[13] Son J, Shin JY, Chun EJ, Jung KH, Park KH, Park SJ. Predicting high coronary artery calcium score from retinal fundus images with deep learning algorithms. Transl Vis Sci Technol 2020;9(2):28. 28.
[14] Rim TH, Lee CJ, Tham YC, Cheung N, Yu M, Lee G, Kim Y, Ting DSW, Chong CCY, Choi YS, Yoo TK, Ryu IH, Baik SJ, Kim YA, Kim SK, Lee SH, Lee BK, Kang SM, Wong EYM, Kim HC, Kim SS, Park S, Cheng CY, Wong TY. Deep-learning-based cardiovascular risk stratification using coronary artery calcium scores predicted from retinal photographs. Lancet Digit Health 2021;3(5):e306–16.
[15] Wang J, Tan GJ, Han LN, Bai YY, He M, Liu HB. Novel biomarkers for cardiovascular risk prediction. J Geriatr Cardiol JGC 2017;14(2):135.
[16] LeCun Y, Bengio Y, Hinton G. Deep learning. Nature 2015;521(7553):436–44.
[17] Esteva A, Kuprel B, Novoa RA, Ko J, Swetter SM, Blau HM, Thrun S. Dermatologist-level classification of skin cancer with deep neural networks. Nature 2017;542(7639):115–8.
[18] Wei Ting DS, Wong TY. Eyeing cardiovascular risk factors. Nat Biomed Eng 2018;2(3):140–1.
[19] Zeleznik R, Foldyna B, Eslami P, Weiss J, Alexander I, Taron J, Parmar C, Alvi RM, Banerji D, Uno M, Kikuchi Y, Karady J, Zhang L, Scholtz JE, Mayrhofer T, Lyass A, Mahoney TF, Massaro JM, Vasan RS, Douglas PS, Hoffmann U, Lu MT, Aerts HJWL. Deep convolutional neural networks to predict cardiovascular risk from computed tomography. Nat Commun 2021;12(1):1–9.
[20] Cheung CY, Xu D, Cheng CY, Sabanayagam C, Tham YC, Yu M, Rim TH, Chai CY, Gopinath B, Mitchell P, Poulton R, Moffitt TE, Caspi A, Yam JC, Tham CC, Jonas JB, Wang YX, Song SJ, Burrell LM, Farouque O, Li LJ, Tan G, Ting DSW, Hsu W, Lee ML, Wong TY. A deep-learning system for the evaluation of cardiovascular disease risk via the measurement of retinal-vessel calibre. Nat Biomed Eng 2021;5(6):498–508.
[21] Ballinger B, Hsieh J, Singh A, Sohoni N, Tison GH, Wang J, Marcus GM, Sanchez JM, Maguire C, Olgin JE, Pletcher MJ. DeepHeart: semi-supervised sequence learning for cardiovascular risk prediction. In: Proceedings of the AAAI conference on artificial intelligence. 32; 2018. April.
[22] 1000 fundus images with 39 categories, "https://www.kaggle.com/linchundan/fundusimage1000", accessed on December 2021.
[23] Mane VM, Jadhav DV. Holoentropy enabled-decision tree for automatic classification of diabetic retinopathy using retinal fundus images. Biomed Eng Biomed Tech 2017;62(3):321–32.
[24] Saha S, Mou L, Qiu C, Zhu XX, Bovolo F, Bruzzone L. Unsupervised deep joint segmentation of multitemporal high-resolution images. IEEE Trans Geosci Remote Sens 2020;58(12):8780–92.
[25] Javaid S, Abdullah M, Javaid N, Sultana T, Ahmed J, Sattar NA. Towards buildings energy management: using seasonal schedules under time of use pricing tariff via deep neuro-fuzzy optimizer. In: Proceedings of the 15th international wireless communications & mobile computing conference (IWCMC); 2019. p. 1594–9. June.
[26] Bhaladhare PR, Jinwala DC. A clustering approach for the-diversity model in privacy preserving data mining using fractional calculus-bacterial foraging optimization algorithm. Adv Comput Eng 2014:1–12.
[27] MiarNaeimi F, Azizyan G, Rashki M. Horse herd optimization algorithm: a nature-inspired algorithm for high-dimensional optimization problems. Knowl Based Syst 2021;213:106711.
[28] Liu G, Zhang S, Xie Z. A novel infrared and visible face fusion recognition method based on non-subsampled contourlet transform. In: Proceedings of the 10th international congress on image and signal processing, BioMedical engineering and informatics (CISP-BMEI). Shanghai, China: IEEE; 2017. p. 1–6.
[29] Chahi A, Ruichek Y, Touahni R. Local directional ternary pattern: a new texture descriptor for texture classification. Comput Vis Image Underst 2018;169:14–27.